

# Ultrahigh Performance Nanoengineered Graphene–Concrete Composites for Multifunctional Applications

*Dimitar Dimov, Iddo Amit, Olivier Gorrie, Matthew D. Barnes, Nicola J. Townsend, Ana I. S. Neves, Freddie Withers, Saverio Russo, and Monica Felicia Craciun\**

There is a constant drive for development of ultrahigh performance multifunctional construction materials by the modern engineering technologies. These materials have to exhibit enhanced durability and mechanical performance, and have to incorporate functionalities that satisfy multiple uses in order to be suitable for future emerging structural applications. There is a wide consensus in the research community that concrete, the most used construction material worldwide, has to be engineered at the nanoscale, where its chemical and physiochemical properties can be truly enhanced. Here, an innovative multifunctional nanoengineered concrete showing an unprecedented range of enhanced properties when compared to standard concrete, is reported. These include an increase of up to 146% in the compressive and 79.5% in the flexural strength, whilst at the same time an enhanced electrical and thermal performance is found. A surprising decrease in water permeability by nearly 400% compared to normal concrete makes this novel composite material ideally suitable for constructions in areas subject to flooding. The unprecedented gamut of functionalities that are reported in this paper are produced by the addition of water-stabilized graphene dispersions, an advancement in the emerging field of nanoengineered concrete which can be readily applied in a more sustainable construction industry.

## 1. Introduction

The new global standards of modern civil technologies, continuously requiring more demanding infrastructure, are driving the development of ultrahigh performance multifunctional construction materials. In particular, extensive efforts are focused on increasing the performance and functionality of concrete, the most used construction material worldwide. A truly step changing approach to enhance mechanical performance and to provide novel functionalities requires intervention at the nanoscale since most of the damage caused to concrete can be

traced back to chemical and mechanical defects in the cement structure. Current research efforts are therefore directed at exploring new ways of enhancing the performance of concrete by nanoengineering the chemical and physico-mechanical properties of cement, the main binding element in the composition of concrete. The cement particles, which consist of a variety of chemical elements (such as calcium silicates, aluminates, and aluminoferrites), undergo transformation from powder form to fibrous crystals upon reacting with water, known as the hydration reaction.<sup>[1]</sup> Their growth and mechanical interlocking over time are the most significant factors in shaping the material properties of concrete. The outstanding chemical and physical properties of nanomaterials provide the most efficient enhancement for the internal matrix of concrete, and recent progress in nanomodification of cement composite materials has enabled applications in structural reinforcement, reduction of environmental pollution,<sup>[2]</sup> and production of self-cleaning materials.<sup>[3]</sup>

Previous studies<sup>[4–10]</sup> have largely focused on the incorporation of nanomaterials in cement. These include the incorporation of carbon nanotubes (CNTs)<sup>[7]</sup> and graphene oxide (GO)<sup>[4,5]</sup> in cement which resulted in a 50% (for CNT) and a 33% (for GO) improvement of the compressive strength, while industrial-grade thin graphite platelets (100 nm thickness)<sup>[6]</sup> were shown to improve the thermal conductivity. However, these findings do not extend directly to concrete, as the addition of sand and aggregate changes the physico-mechanical behavior of the material. Moreover, to date the role of atomically thin materials on nanoengineering of concrete is yet to be explored, and this holds the promise to change the landscape of construction materials leading to a more sustainable urbanization with lower carbon foot print and more resilient constructions against natural disasters.

Here we report innovative few-atoms-thin graphene-enabled nanoengineered multifunctional concrete composites which display an unprecedented range of enhanced properties compared to standard concrete. We demonstrate an extraordinary increase of up to 146% in the compressive strength, up to 79.5% in the flexural one, and a decrease in the maximum displacement due to compressive loading by 78%. At the same

D. Dimov, Dr. I. Amit, O. Gorrie, Dr. M. D. Barnes, N. J. Townsend, Dr. A. I. S. Neves, Dr. F. Withers, Prof. S. Russo, Prof. M. F. Craciun  
Centre for Graphene Science  
College of Engineering, Mathematics and Physical Sciences  
University of Exeter  
Exeter EX4 4QF, UK  
E-mail: m.f.craciun@exeter.ac.uk

 The ORCID identification number(s) for the author(s) of this article can be found under <https://doi.org/10.1002/adfm.201705183>.

DOI: 10.1002/adfm.201705183

time, we find an enhanced electrical and thermal performance with 88% increase in heat capacity. A remarkable decrease in water permeability by nearly 400% compared to the standard concrete, which is an extremely sought-after property for long durability of concrete structures, makes this novel composite material ideally suitable for constructions in areas subject to flooding. Finally, we show that the inclusion of graphene in nowadays concrete would lead to a reduction by 50% of the required concrete material while still fulfilling the specifications for the loading of buildings. This would lead to a significant reduction of 446 kg per tonne of the carbon emissions by the cement manufacturing. Crucially, we demonstrate that the unprecedented gamut of functionalities that we report in this paper are produced by the addition of water-stabilized graphene dispersions, with high yield, low cost, and compatible with the large-scale manufacturing required for the use of this material in practical applications. The unprecedented range of functionalities and properties uncovered in our study represents an advancement in the emerging field of nanoengineered materials which can be readily applied in a more sustainable, environmentally friendly construction industry.

## 2. Results

### 2.1. Fabrication of Water-Dispersed Graphene

Since the isolation of graphene, various methods for large-scale production were demonstrated including chemical vapor deposition,<sup>[11]</sup> chemical exfoliation,<sup>[12]</sup> and liquid phase exfoliation.<sup>[13–16]</sup> The latter allows the separation of graphite into graphene layers in a liquid medium to produce few-layer graphene dispersions, stabilized by a surfactant<sup>[13–15]</sup> or solvents.<sup>[16]</sup> Recent progress in liquid phase exfoliation made by using high-shear blending<sup>[15]</sup> has significantly improved the quality of graphene and the volume–time dependency of exfoliating graphene in water, allowing for production of more than 100 L h<sup>-1</sup> of defect-free graphene solution.<sup>[15]</sup> In this work, we demonstrate that the high-shear exfoliation of graphene in water is extremely efficient for the fabrication of graphene-reinforced concrete as it can substitute water directly in the concrete mixture and it is industrially scalable. We use two types of graphene materials, surfactant functionalized graphene (FG) and commercially available graphene nanoplatelets, both dispersed in water using high-shear blending.

To introduce multifunctionalities to concrete using graphene, we first prepared suspensions of graphene in water by high-shear liquid phase exfoliation of graphite powder using the surfactant sodium cholate (see **Figure 1A**), resulting in surfactant FG. **Figure 1B** shows the high-shear mixer used in this work. The exfoliation process occurs inside the square hole head, shown in the inset of **Figure 1B**, where the rotor blade shears platelets at very high speed (up to 8000 rpm) against the square hole head. When graphite flakes are trapped in the narrow space between the rotor and the head, shear forces developed in the liquid separate the weakly (van der Waals) coupled graphene layers of graphite. The resulting suspension of exfoliated graphene flakes dispersed in water is shown in **Figure 1C**, with the schematic structure of FG illustrated in the

inset of **Figure 1C**. As it has previously been demonstrated, the surfactant can play multiple roles in the preparation of water suspended graphene, i.e., it helps decrease the water surface tension to match that of graphene and make the exfoliation feasible, allows the formation of uniform mixtures of graphite precursor, and most importantly stabilizes the exfoliated graphene nanosheets and prevents them from aggregating.<sup>[13,14]</sup> Suspensions with various concentrations of FG in water were prepared (see **Figure S1** in the Supporting Information) and used for concrete mixing. We have also investigated the incorporation in concrete of ultrathin graphite (UTGr) flakes prepared by the same method as FG in order to establish whether graphene or graphite is the most efficient nanoreinforcement for concrete. Finally, we have incorporated in the concrete commercially available graphene nanoplatelets of industrial grade (IG), by dispersing dried powder in water using the high-shear mixer shown in **Figure 1C**.

Prior to their incorporation in concrete we have characterized graphene (FG and IG) and graphite (UTGr) materials by fabricating thin films which were investigated by optical and scanning electron microscopy (SEM), as well as Raman spectroscopy to determine the number of layers and level of defects. To this end, after decanting the suspension and discarding the heavy excess graphite, the dispersion was filtered through a mixed cellulose hydrophilic Millipore(R) membrane with 0.025 μm pore size. **Figure 1D** shows a continuous film of FG on the filter membrane. The FG was then released from the filter by immersion and floating in water as shown in **Figure 1D** and transferred onto a SiO<sub>2</sub> substrate (see **Figure S1** in the Supporting Information). SEM analysis revealed that the film consists of flakes with sizes ranging from 0.07 up to 1.06 μm<sup>2</sup> in area (for details, see **Figure S3** in the Supporting Information).

Scanning Raman spectroscopy was performed on representative areas of 20 × 20 μm<sup>2</sup> and used to study the number of layers and the nature of defects in the continuous film. **Figure 1E** shows single scans of the 2D peak for FG, UTGr, IG, and bulk graphite. We have estimated the number of layers from the 2D peak shift in graphene relative to graphite, using the method developed by Paton et al. for graphene films obtained from dispersions<sup>[15]</sup> (see the Supporting Information for details). We found that FG graphene consists of flakes with the number of layers that varies from four to seven with the majority of flakes six graphene layers thick (see the map on **Figure 1F**). IG graphene consists of flakes with the number of layers varying between 10 and 14 with the majority of the flakes containing 10–11 graphene layers (see the map on **Figure 1F**). UTGr consists of flakes with the majority of 20–21 layers.

To assess the level of defects, we have measured the D peak (around 1340 cm<sup>-1</sup>), the G peak (around 1600 cm<sup>-1</sup>) and D' peak which is visible as a small shoulder on the right side of G. The intensity ratio of D and G peaks  $I_D/I_G$ , which is one of the parameters used to quantify the defects in graphene, varies between the three different types of graphene. We have studied the range of intensity ratios for UTGr, IG, and FG using Raman maps as shown in **Figure 1G**, showing that defects are present everywhere. We selected one representative scan of each map corresponding to the intensity ratio with highest occurrence (0.08 for UTGr, 0.7 for IG, and 0.53 for FG) and plotted

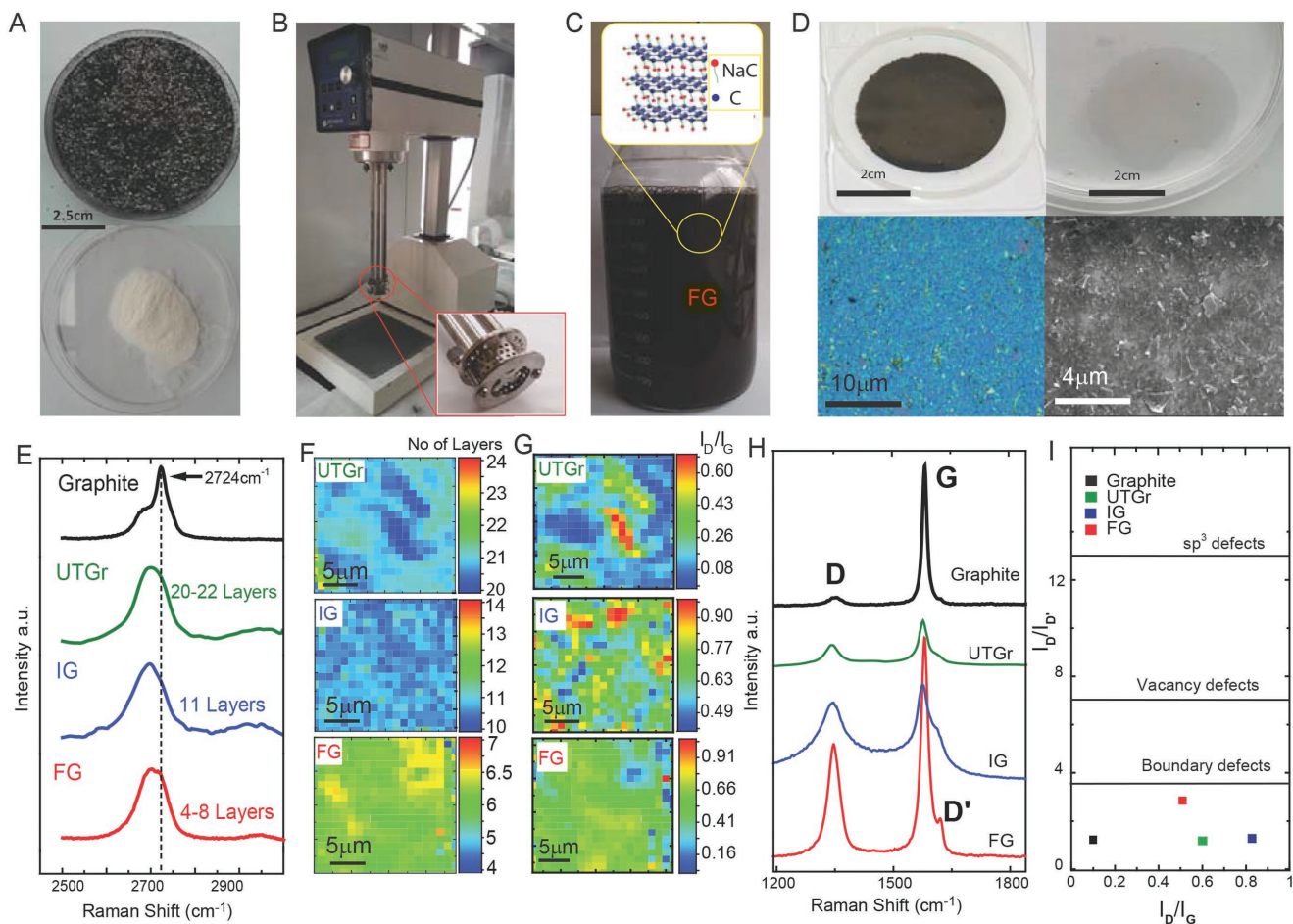


**Figure 1.** Fabrication and characterization of graphene. A) Photograph of graphite flakes and of surfactant sodium cholate used for production of water-dispersed functionalized graphene. B) Photograph of a Silverson L5M laboratory mixer used to obtain the graphene solutions. The inset shows the rotor head of the mixer, with the diameter of the head 32 mm, square holes. C) Photograph of typical surfactant-stabilized graphene solution. The inset is a schematic of the graphene layers functionalized with the surfactant molecules. D) Photographs of membrane with a 0.025  $\mu\text{m}$  filter with deposited surfactant-stabilized graphene dispersions (top left) of continuous graphene film floating on water surface (top right). The bottom panels show optical (left) and scanning electron microscopy (right) images of the graphene film deposited on Si/SiO<sub>2</sub> substrate. E) Comparison of the 2D peak position of graphite and different thicknesses of graphene flakes. F) Raman map of the number of layers across the continuous film. G) Maps showing the  $I_D/I_G$  ratios of a uniform area of the continuous graphene film for each of the three types deposited on SiO<sub>2</sub> substrates. H) One spectrum of each graphene type showing the G, D, and D' peaks in comparison with bulk graphite. I) Plot of the  $I_D/I_D'$  ratios corresponding to the four  $I_D/I_G$  ratios from panel (H) showing that there are no defects introduced to the basal plane of the graphene dispersions.

the single scan, focusing on D, G, and D' peaks as shown on Figure 1H. The relationship between the  $I_D/I_G$  and  $I_D/I_{D'}$  ratios is an effective tool to quantify the nature of defects. Specifically, a ratio around 14 corresponds to  $\text{sp}^3$  defects, whereas  $I_D/I_{D'}$  of 7 and 3.5 correspond to vacancy and boundary defects, respectively.<sup>[17]</sup> As shown in Figure 1I, the  $I_D/I_{D'}$  of  $\approx 2.39$  found in our graphene films demonstrates that for the whole range of  $I_D/I_G$  the level of defects is always below the benchmark for boundary defects. Therefore, we can conclude that the shear mixing does not introduce defects to the basal plane of exfoliated graphene.

## 2.2. Strength of Graphene Nanoengineered Concrete

The high-shear liquid phase exfoliation method used to manufacture water-based graphene dispersions is suitable for

combining graphene with concrete because of the potential for high throughput of the industrial scale equivalent equipment, i.e., in excess of 100 L h<sup>-1</sup>. Thus, we have incorporated graphene into concrete by mixing the water-based graphene dispersions with ordinary Portland cement (OPC), fine dry sand, and 10 mm coarse aggregate; see Figure 2A and Experimental Sections. Various solutions with different concentrations of FG and IG in water were investigated in order to optimize the performance of the graphene-reinforced concrete. Subsequently, cubes of concrete as shown in Figure 2B were prepared, cured, and tested for their compressive strength according to standards regulating the architectural and engineering designs (see Section S7 in the Supporting Information). Specifically, the fresh concrete mix was poured in standard 10 × 10 × 10 cm steel molds, removed after 24 h and kept in a water tank to cure (see Experimental Section and Supporting Information for more details). One of

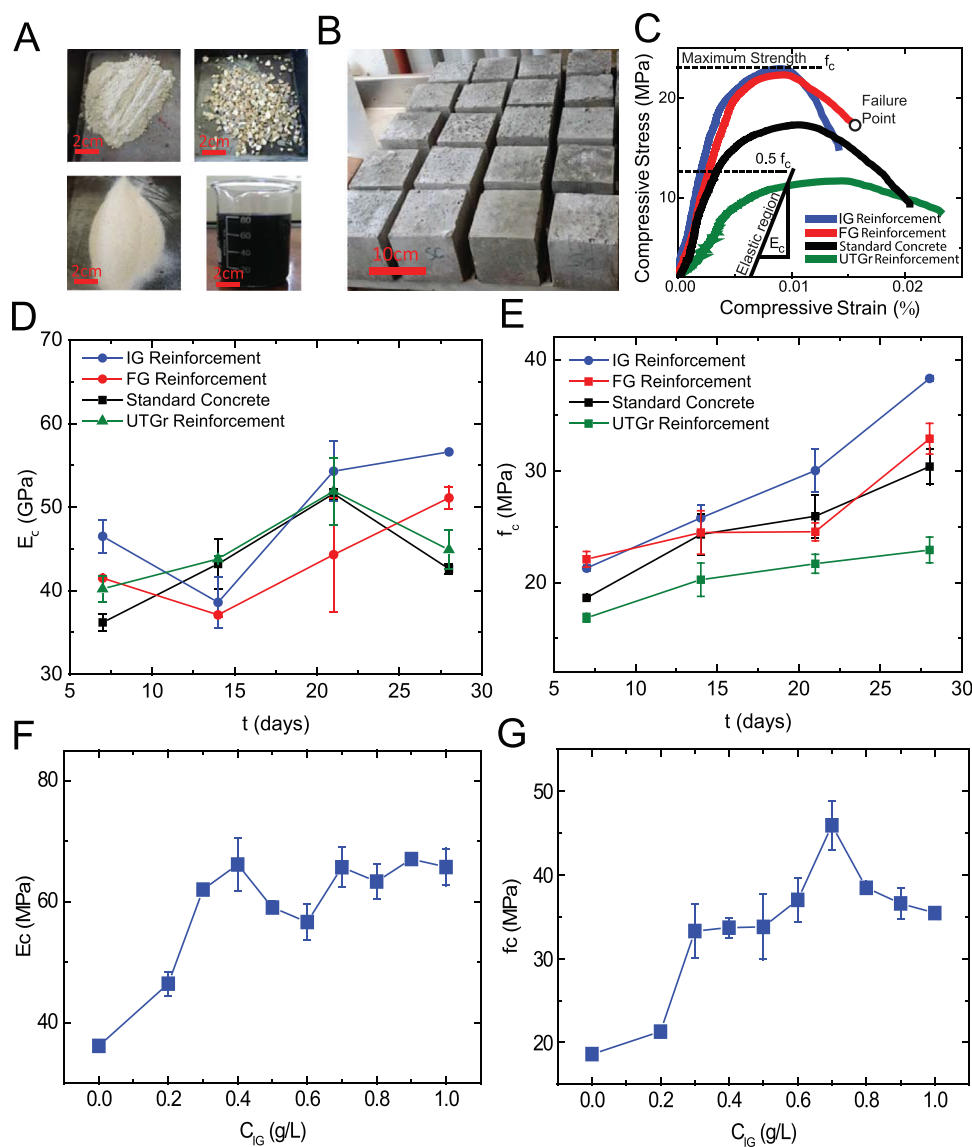


**Figure 2.** Compressive strength of graphene reinforced concrete. A) Materials used for concrete preparation and sample of graphene solution. B) Concrete samples used for testing. C) Typical stress–strain curve of concrete cube measured under compressive loading, comparing the standard concrete with graphene (IG and FG) and graphite (UTGr) reinforcements. D) The evolution of Young’s modulus ( $E_c$ ) over time ( $t$ ) for standard concrete and concrete reinforced with graphene (IG and FG) and graphite (UTGr). E) The evolution of concrete compressive strength ( $f_c$ ), over time ( $t$ ) for standard concrete and concrete reinforced with graphene (IG and FG) and graphite (UTGr). F) Investigation of early age  $E_c$  of concrete (after 7 d of curing) for increasing graphene concentration and G) early age  $f_c$ . Each data point is an average of three cubes.

the key mechanical properties of concrete is the evolution of compressive strength over time. Therefore, we have tested the cubes after intervals of curing time ranging between 7 and 28 d, in order to extract the early age and later age strength values. The graphene-reinforced concrete samples were compared with standard concrete. To this end, a control sample group was produced following the same procedure, but with replacing the graphene water solution with tap water. These measurements ensure that the concrete samples investigated in this work comply with the test batches used for casting at construction sites that are prepared in accordance with engineering designs.

The uniaxial compressive and flexural strength tests on concrete cubes and beams, respectively, are the most widely used

methods for evaluating the fundamental mechanical properties of concrete. Therefore, in the following sections we will focus on these types of measurements to characterize the mechanical properties of graphene-reinforced concrete and evaluate the effectiveness of this type of reinforcement. The compressive stress was determined by dividing the measured applied force by the area of the cube. The strain was obtained from standard mechanical strain gauge. Figure 2C shows typical stress–strain curves that we measured under compressive loading for concrete cubes cured for 7 d and produced using the three different types of concrete: concrete reinforced with IG, FG, and UTGr as well as standard water-based concrete. The stress–strain curve consists of two parts, i.e., the ascending branch

(from 0 to the maximum strength) and the descending branch (from maximum strength to the failure point). The first half of the ascending branch is approximately a straight line and corresponds to the elastic region. This segment is labeled as  $0.5 f_c$ , with  $f_c$  being the maximum strength of the cube. In this region, the deformations due to compressive loading are reversible and mainly caused by slipping between bulk aggregates and cement crystals. The slope of this section gives the Young's modulus ( $E_c$ ) of the material, which is a measure of its stiffness. As it can be seen from Figure 2C, graphene reinforcement results in a steeper elastic region compared to standard concrete, indicating a stiffer material with stronger bonds between cement and aggregates. On the other hand, the reinforcement with ultrathin graphite leads to decrease in the performance, with lowering of the overall strength, while  $E_c$  remains relatively unchanged. This finding suggests that the 24 nm thick graphite particles are hampering the hydration reaction and are blocking the cement crystals form proper interlocking. Figure 2D shows the extracted values for  $E_c$  as a function of curing time. We observed that for early age concrete samples (i.e., after 7 d of curing) both FG- and IG-reinforced concrete have higher  $E_c$  than standard concrete—30.7% and 35.8% increase, respectively, whereas graphite reinforcement leaves the  $E_c$  unchanged. Furthermore, the values measured for later age concrete (i.e., after 28 d of curing) are very similar both in number and percentage increase to the values observed after 7 d of curing. This suggests that durability of the concrete remains stable over time, making it suitable for industrial applications.

Upon increasing the stress above the elastic region, a gradual decrease in the slope of the stress–strain curve is observed. This is the plastic deformation region where the bonds between cement and aggregates still undergo a period of strain hardening, but with nonreversible changes. These effects are due to the viscous flow of hydrated cement paste in concrete, as well as due to the propagation and growth of initial microcracks.<sup>[18]</sup> Also in this region we observe a similar behavior to the elastic region, where graphene-reinforced concrete is stiffer than standard concrete. When the stress is increased closer to the peak point in the stress–strain curve, internal cracks speed their propagation, and the specimen is about to fail. In Figure 2D it is evident that  $f_c$  of graphene-reinforced concrete has higher values than standard concrete whereas graphite reinforcement lowers the  $f_c$  of standard concrete. Figure 2E is a plot of  $f_c$  as a function of curing time, where each data point is an average of three cubes. Seven days after curing, an 18.6% increase in strength is observed for FG reinforcement and 14.3% increase with IG reinforcement, compared to the standard concrete. To further investigate how  $f_c$  of concrete evolves with varying concentration of graphene, we have performed a systematic study of the stress–strain curve for a wide range of graphene concentrations. Figure 2F,G shows the evolution of  $E_c$  and  $f_c$  for IG. The optimal IG concentration was found to be  $0.7 \text{ g L}^{-1}$  and it increases both  $E_c$  and  $f_c$  by 80.5% and 146%, respectively. Similarly, we found that for FG reinforcement the best performance is achieved for  $0.59 \text{ g L}^{-1}$  concentration of FG (see the Supporting Information). These studies demonstrate that reinforcing concrete with graphene, for both types of materials, has significant impact on increasing the early age compressive strength of concrete. With increasing the curing time to 14, 21,

and 28 d, the strength of all the samples continues to increase, with graphene-reinforced concrete remaining stronger than standard concrete. In particular, the testing performed after 28 d of curing reveals that reinforcement with IG results in about 26% stronger concrete than the standard concrete, demonstrating the possibility of later age reinforcement of concrete with graphene.

To further confirm that graphene reinforces concrete, we performed statistical studies by preparing and testing more than 150 concrete cubes. This included batches of 20 samples for each of the 3 experimental groups (Standard Concrete,  $0.59 \text{ g L}^{-1}$  FG, and  $0.7 \text{ g L}^{-1}$  IG), all of them tested for compressive strength after 7 and 28 d of curing. Figure 3A,B shows the statistical study of  $E_c$ , whereas Figure 3C,D shows the study of  $f_c$ , after curing for 7 and 28 d, respectively. These studies confirm the measurements reported in Figure 2D,E and support the conclusion that incorporation of graphene into the concrete matrix increases the compressive strength of both the early and later age concrete.

To better understand the internal deformations and dislocations between cement and aggregate, cyclic loading compression tests were performed, measuring the stress strain curve for five loops of loading and unloading up to 60% of the  $f_c$ . Figure 4A is a plot focusing on the maximum vertical displacement, measured directly from the mechanical strain gauge apparatus, of one sample after each cycle loading. Figure 4A shows that even after multiple loading–deloading patterns, the graphene-reinforced samples do not experience as much internal deformation as standard concrete. As shown in Figure 4B, the overall  $\delta_{\text{max}}$  of the concrete decreases with increasing the concentration of graphene indicating stronger molecular bonds as concrete is being progressively reinforced. We then focus on the first loop of the  $F$ – $\delta$  plot to study the maximum plastic strain  $\epsilon_{\text{pl}}$ . The method derived by Mander et al.<sup>[19]</sup> was used to calculate  $\epsilon_{\text{pl}}$ —it lies on the secant line of the unloading curve (the black line) of the loop, as shown in Figure 4C. The plastic strain indicates the residual deformation when the applied stresses are removed. As it can be seen from Figure 4D, for the whole range of graphene concentrations, the reinforcement helps to decrease the  $\epsilon_{\text{pl}}$  when compared to standard concrete (i.e.,  $C_{\text{IG}} = 0$ ) which is in agreement with overall increase in  $f_c$  and  $E_c$ .

After having established that graphene reinforcement increases the compressive strength of concrete, we now turn our attention to the study of flexural strength ( $f_{\text{cr}}$ ) of graphene-reinforced concrete. The most common method for testing and calculating  $f_{\text{cr}}$  is the 3-point bending test which is performed on rectangular beams with dimensions of  $10 \times 10 \times 400 \text{ cm}$  as shown in Figure 5A. The force is applied at the center of the beam which is resting on two supports at equal distance from the center point. The mid-span deflection  $\delta$  is measured using displacement transducer in order to give better understanding of the flexural modulus ( $E_{\text{cr}}$ ). Beams were prepared for standard concrete and for different IG concentrations and tested after 7 and after 28 d of curing. Figure 5B shows typical stress–strain curves extracted from the 3-point bending test after 7 d of specimen curing. The flexural strength is given by the maximum flexural stress. Similarly to the compressive modulus of elasticity, the flexural one is also dependent on the slope of the tangent line of the first 50% of the curve; however,

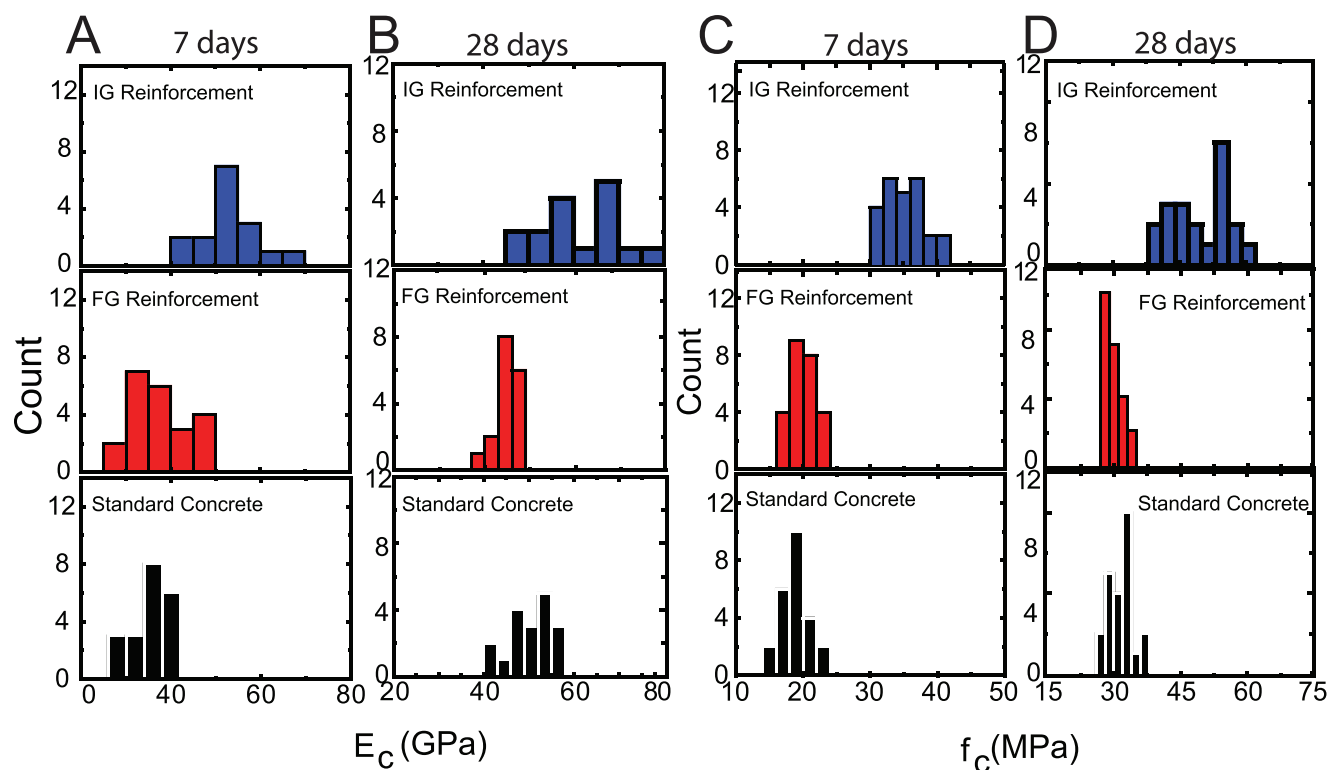


**Figure 3.** Statistical study of compressive strength of graphene-reinforced concrete. A) Statistical study on Young's modulus of the material ( $E_c$ ) after 7 d and B) after 28 d of  $0.7 \text{ g L}^{-1}$  IG, FG, and standard concrete experimental groups. C) The same statistical study of the compressive strength ( $f_c$ ) after 7 d and D) after 28 d.

it includes the second moment of area too (see the Supporting Information for details).

Figure 5C and Figure 5E show the  $E_{cr}$  and  $f_{cr}$  of standard concrete and IG-reinforced concrete beams, respectively, after 7 d of curing. Clearly as the graphene concentration is increased, both properties are improved, showing maximum increase with IG concentration of  $0.6 \text{ g L}^{-1}$ —21.8% and 18.6% for  $E_{cr}$  and  $f_{cr}$ , respectively. 28 d after specimen curing the mechanical improvement is still present with 78.5% increase in  $E_{cr}$  and 79% for  $f_{cr}$  as shown in Figure 5D,F for the same IG concentration. This massive increase in flexural modulus and strength are in agreement with the increase of maximum  $f_c$  and decrease of compressive  $\delta_{max}$  shown in previous figures.

As we will now discuss, the observed strengthening of concrete by incorporation of graphene can be interpreted in terms of the modification of cement hydration reaction. To understand the details of our discussion, it is important to recall some basic aspects of this reaction and relevant properties of graphene. Concrete is composed of fine and bulk aggregate, mechanically interlocked as a result of the hydration reaction between cement and water. Upon reacting with water molecules, the cement microcrystalline powder undergoes physical transformations to fibrous crystals containing mainly calcium silicates, aluminoferrites, and calcium hydroxide ( $\text{Ca}(\text{OH})_2$ ). More than 40 variations of silicate crystals have been reported to occur in the composition of cement<sup>[20]</sup> and they form the calcium silicate hydrate (C–S–H) gel, which is one of the main elements responsible for the mechanical properties of concrete. Graphene is a crystalline sheet of carbon atoms,

packed in a hexagonal structure. Graphene monolayers and few-layers have a large specific surface area and high Young's modulus ( $E_c$  around  $2 \text{ TPa}$ <sup>[21]</sup>). As it has already been demonstrated, graphene interacts with various elements forming the vast elements C–S–H groups<sup>[20]</sup> and alters the morphology of the hydration crystals.<sup>[6]</sup> In particular, due to the high surface energy of graphene, C–S–H particles bond to graphene and act as nucleation sites, promoting the growth of C–S–H gels along the graphene flakes. This process leads to an increase in the bond strength of cement.<sup>[22]</sup> As we have demonstrated in Figure 3, the defects found in our graphene materials are only due to boundaries of the flakes. Therefore, the defect-free basal plane of our graphene material forms an ideal platform for the growth of C–S–H crystals with higher degree of crystallinity than the crystals occurring in the standard concrete. The degree of crystallinity is one of the most important physical parameters responsible for the mechanical properties of a material and determines various parameters, such as the Young's modulus and strength. Indeed, we have performed X-ray diffraction (XRD) (see Section S11 in the Supporting Information) which indicates a modification of the cement crystals upon graphene incorporation, more specifically to calcium aluminoferrite, calcium carbonate, tri- and di-calcium silicates as well as calcium aluminate groups. We believe that these microstructural changes in the crystals at the very early stages of hydration are responsible for the ultrahigh strength of the concrete at later stages (7 and 28 d). Furthermore, combining C–S–H which has an  $E_c$  of  $23.8 \text{ GPa}$ <sup>[23]</sup> with graphene ( $E_c$  of  $2 \text{ TPa}$ ) would lead to a considerable increase in the  $E_c$  of the composite material.

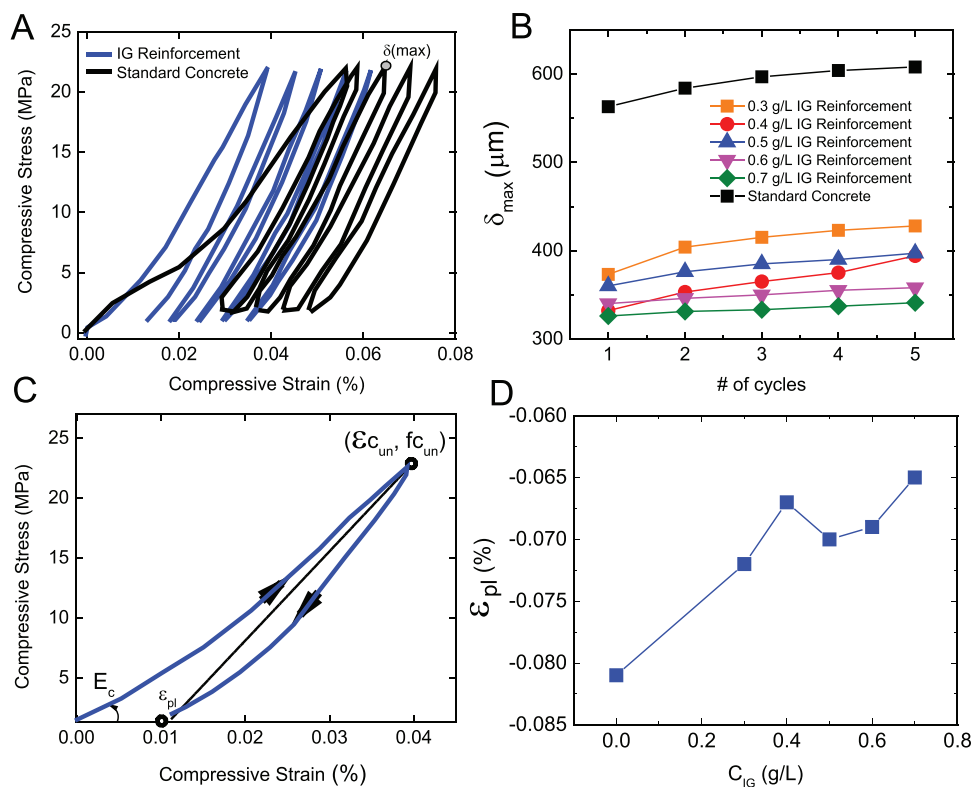


**Figure 4.** Cycling loading compressive tests of graphene-reinforced concrete. A) Measurement showing typical stress–strain relationship of cycling loading compressive tests on a concrete cube. The loops have been spaced out by  $\Delta(100\ \mu\text{m})$  for better reading and the maximum displacement ( $\delta_{\text{max}}$ ) of each loop has been highlighted in red. B) Comparison of the maximum displacement under compressive cycling loading for reinforced cubes with increasing graphene concentration. C) The first loop of the cyclic loading measurement is extracted to study the unloading curve. The maximum plastic strain is calculated from the secant line of the unloading curve. D) The evolution of the plastic strain as a function of increased graphene concentration in the reinforced concrete samples.

Therefore, we believe that the possible formation of C–S–H crystals along the graphene flakes with high degree of crystallinity combined with the high Young’s modulus of graphene could lead to a stiffer graphene–(C–S–H) composite material than C–S–H alone, as observed experimentally.

Another factor which determines the compressive strength of concrete is the degree of porosity, which results in empty voids within the cement paste due to unhydrated crystals or leaching of  $\text{Ca}(\text{OH})_2$ .  $\text{Ca}(\text{OH})_2$  crystals tend to form on a nanoscale level and, due to their high solubility, leach out when concrete is exposed to fresh water. This process increases the porosity of concrete and, therefore, decreases its strength. We believe that graphene reinforcement could also have an effect on decreasing the degree of porosity. Indeed, previous studies have shown that the microstructure of cement paste is finer and denser with the inclusion of graphene oxide sheets, resulting in an enhancement of its strength and durability.<sup>[4]</sup>

### 2.3. Water Permeability of Graphene Nanoengineered Concrete

To gain further understanding into the durability of concrete and, in particular, whether graphene reinforcement plays any critical role in enhancing it, we have performed water permeability studies. In general, the durability of concrete depends on

the capacity of a fluid to penetrate its microstructure. Degradation mechanisms of concrete often depend on whether water can penetrate into the concrete, possibly causing damage. To investigate the water permeability, we compared the water penetration in samples made of standard and IG-reinforced concrete using the same IG concentrations to those presented in Figure 5. The samples were cured for 7 d, fully dried and immersed in water up to the level as schematically shown in Figure 6A. The black lines in Figure 6A show the level to which the water has infiltrated through the concrete structure after 7 d of immersion in water. It is evident that water penetrates to a lower level in the concrete reinforced with graphene than in standard concrete. Furthermore, the length over which water infiltrates decreases with increasing the concentration of graphene, as apparent in Figure 6A. This effect is also visible in Figure 6B which plots the maximum distance ( $\kappa$ ) between the initial water level and the infiltration level as a function of graphene concentration. Thus, concrete reinforced with graphene acts as a barrier against water infiltration. In particular, a concentration of  $0.8\ \text{g L}^{-1}$  of graphene decreases water permeability of concrete by up to  $\approx 400\%$ . These findings suggest that the enhanced formation of nucleation sites for the C–S–H hydration crystals and the high surface of graphene form a denser network of interlocked cement crystals which not only increases the mechanical properties of concrete but also acts as

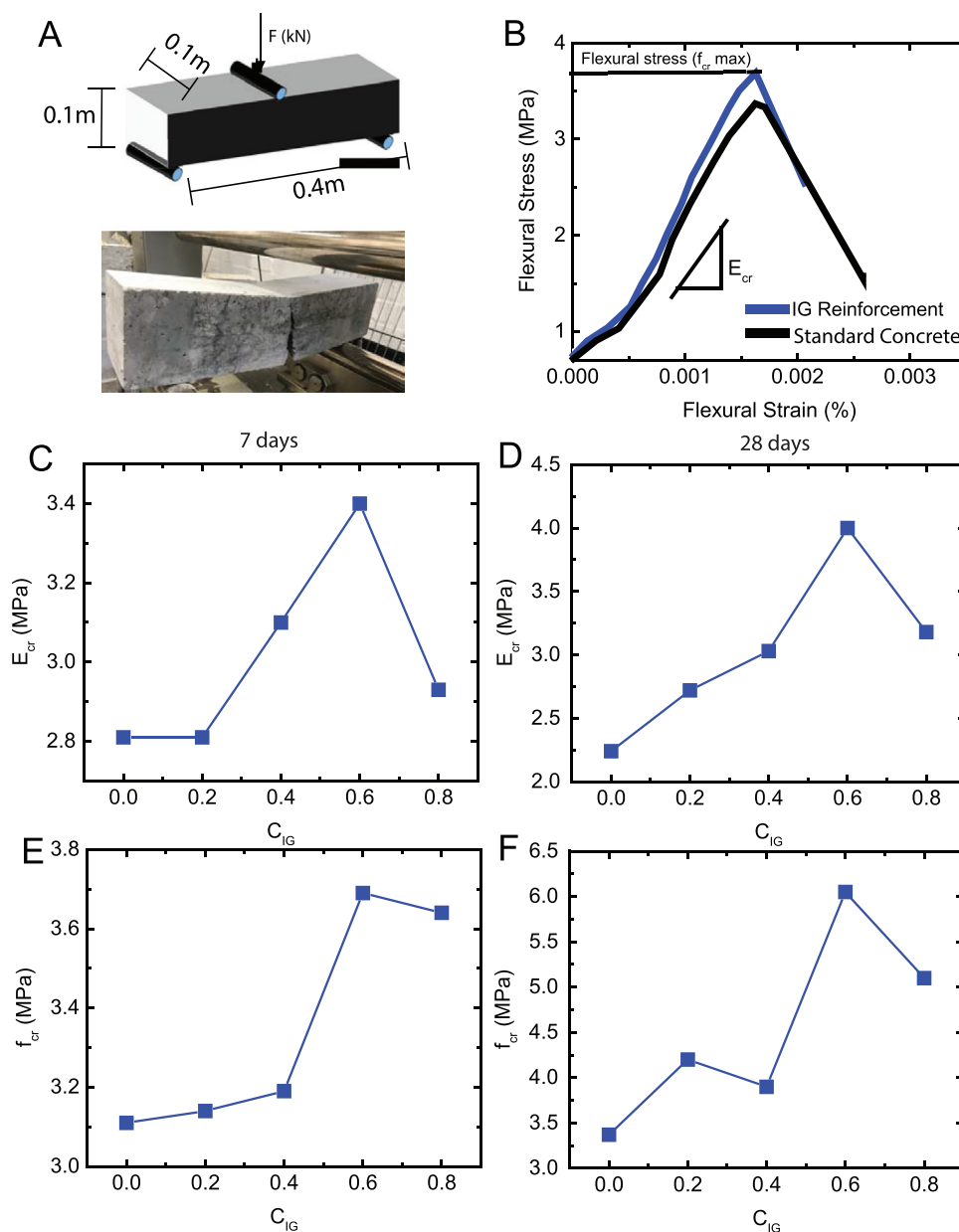


**Figure 5.** Flexural strength of graphene-reinforced concrete. A) Top: schematic showing a typical 3-point bending test for measuring the flexural properties of a concrete beam. Bottom: photograph of the actual concrete beam after failure. B) Typical stress–strain curve under flexural loading showing the maximum flexural stress and strain  $f_{cr}$  of both the standard concrete and the graphene reinforced one (IG). C) Evolution of early age flexural modulus ( $E_{cr}$ ) with increasing graphene concentration  $C_{IG}$  in IG-reinforced concrete. D) Evolution of late age flexural modulus ( $E_{cr}$ ) with increasing graphene concentration  $C_{IG}$  in IG reinforced concrete. (E) Evolution of early age flexural strength  $f_{cr}$  with increasing graphene concentration  $C_{IG}$  in IG-reinforced concrete. F) Evolution of late age flexural strength  $f_{cr}$  with increasing graphene concentration  $C_{IG}$  in IG-reinforced concrete.

a water infiltration barrier and drastically decrease the amount of water that can penetrate the concrete matrix through capillary pores or crack voids. This property is extremely important for the long durability of concrete and, in particular, for the prevention of alkali–silica reaction (ASR), a swelling reaction that occurs in the presence of moisture between the highly alkaline cement paste and the reactive amorphous silica, resulting in serious cracking and critical structural problems. Indeed, ASR can be prevented by a watertight graphene-reinforced concrete barrier which could stop the evolution of the reaction.<sup>[24]</sup>

#### 2.4. Electrical and Thermal Properties of Graphene Nanoengineered Concrete

The decreased water permeability of concrete reinforced with graphene could have profound consequences on its electric properties. Indeed, resistivity measurement is a common test for identifying damp in concrete structures, which typically show enhanced electrical conductivity in the presence of moisture infiltration. To quantify the effects of the addition of graphene to the cement and concrete on their electric properties,

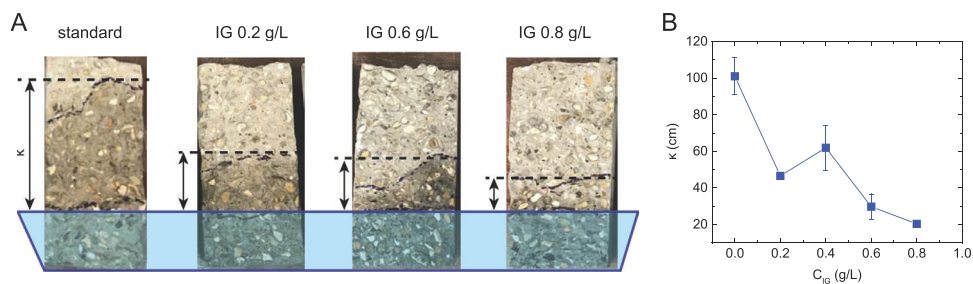


**Figure 6.** Water impermeability of graphene-reinforced concrete. A) Photographs of concrete structures tested for permeability after 7 d in water. B) The maximum depth of water penetration in the standard concrete and graphene-reinforced (IG) concrete for the tested concrete structures.

we have measured the resistivity and the temperature profile of several cement mixtures, with IG concentrations ranging from 0 (as reference) to 8 g L<sup>-1</sup>, upon application of electric bias. The cement was molded into a 4 × 4 × 15 cm bar mold and the concrete into a 10 × 10 × 10 cm cube molds. **Figure 7A,B** shows the measurement configuration for four-probe resistivity measurement and resistive heating measurements, respectively. For the four-probe measurements, the samples are biased using the outer electrodes with a source-measurement unit that also measures the current, as schematically shown in **Figure 7A**. The interelectrode distance ( $l_{2p}$ ) is 12 and 7 cm for the cement bars and concrete cubes, respectively. While biasing the sample, the potential difference between the two inner electrodes ( $V_{4p}$ ) is measured using a voltmeter. Using the known interelectrode

distance for the inner electrodes ( $l_{4p}$ ), the sample's resistivity ( $\rho$ ) is given by  $\rho = (A \cdot V_{4p}) / (I \cdot l_{4p})$ , where  $I$  is the measured current. The total sample resistance ( $R$ ) can then be calculated from  $R = \rho \cdot l_{2p} / A$ , whereas the contact resistance ( $R_c$ ) can be estimated from  $R_c = (V_A / I - R) / 2$ , where  $V_A$  is the applied bias. The results of the  $I$ - $V$  sweeps, shown in **Figure 7C**, give the first indication of an increased resistivity with increased concentration of IG. The curves are plotted for concentrations of 0–1 g L<sup>-1</sup> IG, with increasing concentration marked by the direction of the arrow, and show a steadily decreasing slope which suggests that the overall resistance in the circuit ( $R_t = 2R_c + R$ ) is monotonously rising with the IG concentration. However, due to the nature of the conduction mechanism in concrete, which is predominantly governed by ionic drift, the

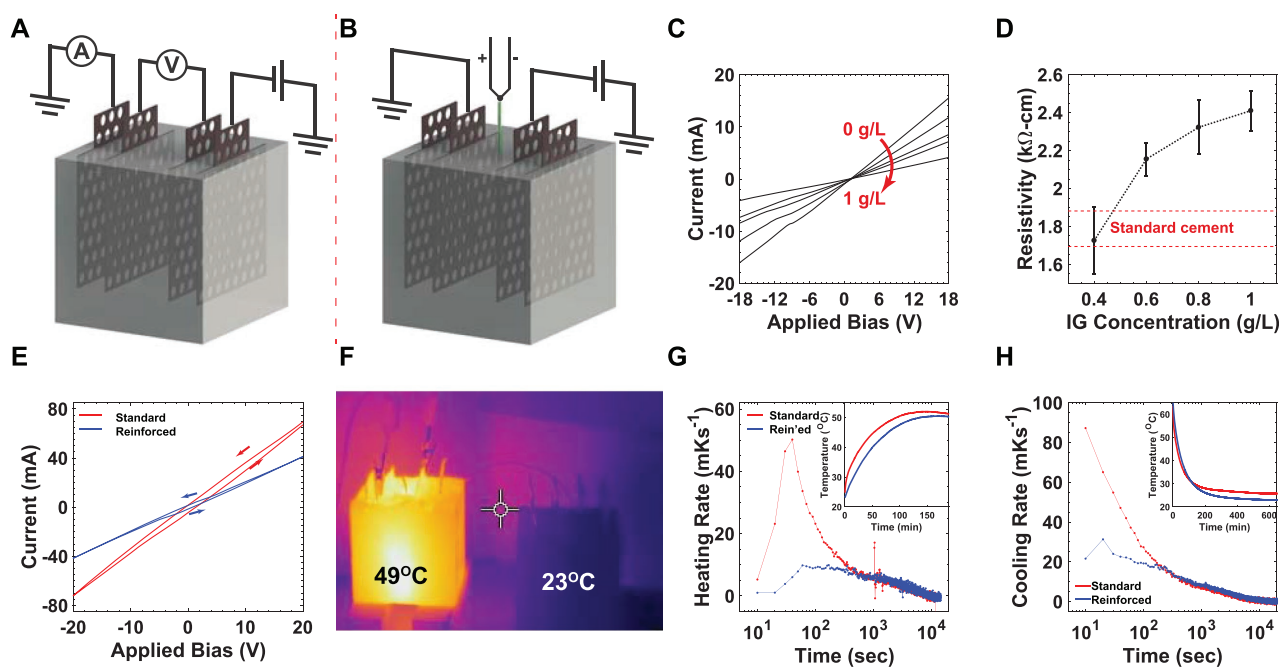


**Figure 7.** Electrical and thermal properties of graphene-reinforced concrete. A) Schematic illustration of a concrete cube showing the embedded electrodes (not to scale) and the electric four-probe configuration used to measure the resistivity. B) The electric configuration used to heat up the cubes and measure the developing temperature profile. C) Current–voltage ( $I$ - $V$ ) curves measured on cement bars with various concentrations of IG ranging from 0 to 1 g L<sup>-1</sup>. The arrow shows the direction of increasing IG concentration. D) Equilibrium resistivity measured on cement bars with IG concentration ranging from 0.4 to 1 g L<sup>-1</sup>. The red dashes show the resistivity obtained in standard cement. E)  $I$ - $V$  sweeps of standard concrete (red) and graphene-reinforced concrete (blue) using 8 g L<sup>-1</sup> IG concentration. F) Thermal image of graphene-reinforced concrete cube biased with 50 V over 3 h (left), and a reference unbiased cube (right). G) Heating rate of standard (red) and graphene-reinforced (blue) concrete cubes shown on a semi-logarithmic scale for clarity. The inset shows the heating curves for both samples. H) Cooling rate of standard and graphene-reinforced concrete cubes, shown on a semi-logarithmic scale using the same color convention from panel (G). The inset shows the cooling curves obtained for both samples.

slope of the  $I$ - $V$  curve as well as the hysteresis around 0 V are dependent on the sweep rate. To exclude the time-dependent contribution, we have measured the steady-state resistivity by allowing the system to reach a constant current over a period of 10 min. The measured currents and potential drops over the last 60 s were then averaged and used to determine the samples' resistivity, which is shown in Figure 7D. In contrast to the  $I$ - $V$  sweeps, the steady-state resistivity shows an increase in resistivity that saturates under 3 k $\Omega$  cm. The increase in resistivity suggests a hindering effect that could be caused by graphene which prevents water ingress. This, in turn, means that the compound is depleted of ions that are responsible for drift current, resulting in a diminished conductivity. It is important to note, however, that the estimated contact resistance remains relatively constant for the different concentrations and ranges between 10 and 50  $\Omega$  for the different samples, without showing a clear trend.

The relatively low resistivity of the graphene-reinforced concrete suggests that it can be readily utilized as a resistive heater for various applications. It is well known that resistive (Joule) heating occurs when a current is passed through a resistor and that the output heat ( $W$ ) is given by  $W = IV = V^2/R$ , where  $V$  is the applied bias,  $I$  is the induced current, and  $R$  is the resistance. However, since the difference in resistance between standard concrete and graphene-reinforced concrete is relatively small, as suggested by the  $I$ - $V$  sweeps in Figure 7E, it is expected that the power output of a standard cube will be relatively similar to that of a reinforced one. To maximize the power output, the cubes were biased using the inner electrodes, resulting in a lower resistance, for long periods of time, while the temperature was monitored continuously using an embedded thermocouple positioned half way between the inner electrodes. The surface temperature of the cubes was monitored periodically using a thermal camera. Figure 7F shows a graphene-reinforced cube with an IG concentration of 8 g L<sup>-1</sup> after it has been biased for 3 h at 50 V on the left, and a reference unbiased cube at room temperature on the right. The striking difference in the thermal properties of the different concrete cubes is revealed when examining the heating (Figure 7G) and cooling (Figure 7H) rates of the cubes. The measurements show that both cubes follow a Newtonian cooling cycle:  $dT/dt = k(T - T_0)$ , where  $T$  is the instantaneous temperature,  $T_0$  is the final (room) temperature,  $t$  is the time, and  $k$  is a constant that depends on the thermal conductivity and heat capacity of the sample, as well as on the sample geometry. The Newtonian cooling cycle indicates that the emission of heat from the sample is dominated by conduction to the surrounding environment (as opposed to convection) which is the same mechanism by which the samples heat up. While the samples reach the same steady-state temperature over long periods of time, it is clear that the heating and cooling rate of the graphene-reinforced cube is substantially lower than that of standard concrete. As discussed before, the lower temperature change rate can be a consequence of lower thermal conductivity, higher heat capacity, or a combination of both. However, the thermal imaging reveals that the spatial heat profile that develops across the surface of the two cubes is qualitatively similar, suggesting that the addition of graphene contributes to the concrete's thermal stability mainly through the increase in heat capacity.

The observed resistivity of graphene-reinforced concrete is also crucial for preventing corrosion when steel rebars are used as conventional reinforcement. This potential corrosion of steel, which is an electrochemical process forming corrosion cells, causes deterioration of steel-reinforced concrete beams or columns through expansion, cracking, and eventual spalling of the steel rebars' cover.<sup>[25]</sup> This decreases the bond strength between steel and concrete, thus leading to several damage to the overall structure. This incidence of damage is especially large in the structures exposed to deicing chemicals.<sup>[25]</sup> However, due to its resistive heater behavior, graphene-reinforced concrete can exclude the addition of such chemicals and yet keep the corrosion formation to minimum in cases when steel embedding is required.

### 3. Discussion

Previous studies<sup>[4-6,8-10]</sup> on nanoengineering cement through the incorporation of nanomaterials such as CNTs, GO, hexagonal boron nitride (hBN), and graphite have shown improvements on the strength and thermal properties. However, the conventional approach to disperse nanomaterials in the dry cement matrix powder is costly, involves complex procedures, difficult to scale up, and can lead to degradation of the mechanical properties of concrete. Progress on reinforcing cement materials with CNT is largely hampered by their chemical incompatibility with cement hydrates.<sup>[26,27]</sup> Likewise, while promising advancements have been made on GO-cement nanocomposites,<sup>[4]</sup> GO reinforcement of concrete still poses major challenges. For example, GO is hydrophilic enough to absorb most of the water contained in the cement mortar, and it has been shown to hamper the proper hydration of the cement, making dispersion of the GO within the matrix difficult. The multiple steps and additives linked to the oxidation change the molecular structure of GO sheets and can introduce defects, resulting in further uncertainties in the GO-cement molecular interactions. The cost-ineffectiveness of the method<sup>[4]</sup> used for the preparation of GO-cement nanocomposites turns the production of GO-cement into a nonviable method for industrial scale production. Finally, most of the previous studies were performed on small samples of GO-cement composites that cannot be directly applied to concrete, as the addition of sand and aggregate changes the physico-mechanical behavior of the material.

The results presented here indicate that nanoengineering concrete through reinforcement with graphene leads to concrete composites with ultrahigh strength and at the same time it widens the range of functionalities. These materials will be of particular interest for the construction industry to develop new competitive structural applications. Besides enhancing the mechanical performance, we demonstrate that the novel graphene-concrete composites satisfy multiple uses, with the added functionalities derived from the intrinsic properties of graphene. Thus, we show that graphene-concrete composites act as a barrier against water infiltration, which is an extremely desired property for long durability of concrete structures. In addition, we demonstrate enhanced thermal stability mainly through the increase in heat capacity of concrete by incorporation of graphene.

More importantly, it is evident that graphene-reinforced concrete will have positive impact on the environment. First, when compared to other reinforcement methods such as carbon nanotubes and graphene oxide, our method of production and final product are nonhazardous. This, along with the decreasing price of graphene, due to its continuous production scaling up would allow the direct fabrication and incorporation of graphene-reinforced concrete in the construction industry. Another way in which graphene-reinforced concrete will have a positive impact on the environment is by contributing to the decrease of carbon emissions due to cement manufacturing. Specifically, the production of concrete accounts for up to 7% of the global CO<sub>2</sub> emissions.<sup>[28]</sup> We estimate that reducing the quantity of cement by 50% of the required concrete material, while still fulfilling the specifications for the loading of buildings, would lead to a significant reduction of 446 kg per tonne of the carbon emissions by the cement manufacturing (see Section S10 in the Supporting Information). These considerations make our graphene-reinforced concrete a promising material for a better, more environmentally friendly construction industry.

## 4. Experimental Section

**Liquid Exfoliation of Graphene:** Various initial amounts of graphite flakes and surfactant sodium cholate (both supplied by Sigma Aldrich) were exfoliated using a Silverson L5M shear mixer for 2 h at 5000 rpm. Same exfoliation speed and time were used for the industrial grade 3 graphene nanoplatelets (supplied by cheaptubes.com). Both materials were mixed in a beaker using tap water.

**Raman Measurements:** Raman spectra were collected in a Renishaw spectrometer with an excitation laser wavelength of 532 nm, focused to a spot size of 1 μm diameter and ×50 objective lens.

**SEM Measurements:** SEM images were collected with a Phillips SEM. An acceleration voltage of 10 kV, a magnification of ×20 000, and a beam current of 0.13 nA were used.

**Cubes' Preparation and Testing:** To prepare the concrete cube samples, ordinary Portland cement Type II, fine dry sand, and 10 mm coarse aggregate were used with a ratio of 1:2:3, respectively. The water/cement ratio for all batches was kept the same—0.57. Mixing time of the concrete batch was 10 min and the molds were shaken for 6 min using standard vibrating machine. The cubes were demolded 24 h after preparation and were taken out of the water tank 24 h prior to testing. The tests were performed using standard compressive loading apparatus supplied by Controls Group, with constant loading on specimens of 1000 N s<sup>-1</sup>.

**Beams' Preparation and Testing:** To prepare the concrete beams, ordinary Portland cement Type II, fine dry sand, and 10 mm coarse aggregate were used with a ratio of 1:2:3, respectively. The water/cement ratio for all batches was kept the same—0.5. Mixing time of the concrete batch was 10 min and the molds were shaken for 6 min using standard vibrating machine. The beams were demolded 24 h after preparation and were taken out of the water tank 24 h prior to testing. The tests were performed using standard 3-point bending apparatus supplied by Controls Group, with constant loading on specimens of 100 N s<sup>-1</sup>.

**Characterization of Cement and Concrete Resistivity:** Cement bars and concrete cubes were prepared in a mold to test the material's resistivity. The cement mixture was prepared in a similar way to the mixture used for mechanical testing, with varying concentration of IG in the water, ranging from 0 (reference) to 8 g L<sup>-1</sup>. The cement bars were 15 cm long with a cross-section area of 4×4 cm, whereas the concrete cubes were 10×10×10 cm. After the cast has hardened, the samples were cured in water at 40 °C for 7 d and allowed to dry for a day in ambient conditions prior to their measurements. To facilitate the electric characterization,

four copper mesh electrodes were embedded in each cast keeping a distance of 7 and 4 cm between the inner electrodes, and 12 and 7 cm between the outer electrodes of the bars and cubes, respectively. For each mold, the area of the electrodes was 1 cm smaller in width and height than the cross section of the mold to allow the electrodes to be fully embedded without protruding through the surface. The top part of the copper mesh was kept longer to allow for electric connections. To measure resistivity, the outer electrodes were voltage biased between -20 and +20 V, with the current measured over 10 min to allow for the system to stabilize. The potential drop between two inner electrodes was monitored by a voltmeter.

**Heating and Cooling of Concrete:** In some of the cement bars and concrete cubes, a K-type thermocouple was embedded in equal distance between the two inner electrodes. The inner electrodes were then biased using a power generator outputting up to 40 W of power over several hours while the thermocouple was monitored constantly. Thermal images were acquired using an infrared camera from FLIR Systems.

## Supporting Information

Supporting Information is available from the Wiley Online Library or from the author.

## Acknowledgements

The authors acknowledge Ian Moon, Siobhan Kelly, Julian Yates, and Roger Perrett for the technical support in the concrete laboratories. D.D. acknowledges fruitful discussions with Lachlan Marnham. The authors also acknowledge financial support from EPSRC (Grant Nos: EP/J000396/1, EP/K017160, EP/K010050/1, EP/G036101/1, EP/M002438/1, and EP/M001024/1), from the Royal Society Travel Exchange Grants 2012 and 2013, from the European Commission (H2020-MSC-IF-2015-704963 and H2020-MSC-IF-2015-701704) and from the Royal Academy of Engineering.

D.D. conceived the project, designed the experiments, prepared and tested the water-dispersed graphene, and all of the various concrete structures investigated. I.A. performed the measurements and analysis of the electrical and thermal properties of cement and concrete samples, took and analyzed the SEM micrographs. N.J.T. contributed to the design of the electrical and thermal characterization experiments and to the analysis of conductive cement and concrete samples. O.G. prepared and tested cube samples for cycle-loading analysis, A.I.S.N. contributed to the preparation of water-dispersed graphene, prepared figures for the Supporting Information, and contributed to the discussion. M.D.B. contributed to the analysis of the Raman measurement. F.W. contributed to water permeability study. S.R. and M.F.C. directed and supervised the project. D.D. and M.F.C. wrote the paper with input from all authors. All data needed to evaluate the conclusions in the paper were present in the paper and/or the Supporting Information. Additional data related to this paper may be requested from the authors.

## Conflict of Interest

The authors declare no conflict of interest.

## Keywords

graphene, nanoengineered concrete, ultrahigh performance composites, water impermeable concrete

Received: September 8, 2017

Revised: March 2, 2018

Published online: April 23, 2018

- [1] F. M. Lea, *The Chemistry of Cement and Concrete*, Chemical Pub. Co., New York, NY **1970**.
- [2] J. Lee, S. Mahendra, P. J. J. Alvarez, *ACS Nano* **2010**, *7*, 4.
- [3] N. Silvestre, J. de Brito, *Eur. J. Environ. Civ. Eng.* **2015**, *20*, 4.
- [4] Z. Pan, L. He, L. Qiu, A. Korayem, G. Li, J. W. Zhu, F. Collins, D. Li, W. H. Duan, *Cem. Concr. Compos.* **2015**, *58*, 140.
- [5] E. Horszczaruk, E. Mijowska, R. J. Kalenczuk, M. Aleksandrak, S. Mijowska, *Cem. Concr. Compos.* **2015**, *78*, 1.
- [6] A. Sedaghat, M. K. Ram, A. Zayed, R. Kamal, N. Shanahan, *Open J. Compos. Mater.* **2014**, *4*, 1.
- [7] S. Chuah, Z. Pan, J. G. Sanjayan, C. M. Wang, W. H. Duan, *Constr. Build. Mater.* **2014**, *73*, 113.
- [8] Md. A. Rafee, T. N. Narayanan, D. P. Hashim, N. Sakhavand, R. Shahsavari, R. Vajtai, P. M. Ajayan, *Adv. Funct. Mater.* **2013**, *23*, 5624.
- [9] F. Babak, H. Abolfazl, R. Alimorad, G. Parviz, *Sci. World J.* **2014**, *27*, 6323.
- [10] M. L. Cao, H. X. Zhang, C. Zhang, *J. Cent. South Univ.* **2016**, *23*, 919.
- [11] T. Bointon, M. Barnes, S. Russo, M. F. Craciun, *Adv. Mater.* **2015**, *28*, 4200.
- [12] S. Lee, S. H. Eom, J. S. Chung, S. Hur, *Chem. Eng. J.* **2013**, *233*, 297.
- [13] M. Lotya, Y. Hernandez, P. J. King, R. J. Smith, V. Nicolosi, L. S. Karlsson, F. M. Blighe, S. De, Z. Wang, I. T. McGovern, G. S. Duesberg, J. N. Coleman, *J. Am. Chem. Soc.* **2009**, *131*, 3611.
- [14] M. Lotya, P. J. King, U. Khan, S. De, J. N. Coleman, *ACS Nano* **2010**, *6*, 3155.
- [15] K. R. Paton, E. Varrla, C. Backes, R. J. Smith, U. Khan, A. O'Neill, C. Boland, M. Lotya, O. M. Istrate, P. King, T. Higgins, S. Barwich, P. May, P. Puczkarski, I. Ahmed, M. Moebius, H. Pettersson, E. Long, J. Coelho, S. E. O'Brien, E. K. McGuire, B. M. Sanchez, G. S. Duesberg, N. McEvoy, T. J. Pennycook, C. Downing, A. Crossley, V. Nicolosi, J. N. Coleman, *Nat. Mater.* **2014**, *13*, 624.
- [16] W. Liu, B. Xia, X. Wang, J. Wang, *Front. Mater. Sci.* **2012**, *6*, 176.
- [17] A. Eckmann, A. Felten, A. Mishchenko, L. Britnell, R. Krupke, K. S. Novoselov, C. Casiraghi, *Nano Lett.* **2012**, *12*, 3925.
- [18] X. Gu, *Basic Properties of Concrete Structures*, Springer, Berlin **2016**.
- [19] J. B. Mander, M. J. N. Priestley, R. Park, *J. Struct. Eng.* **1988**, *114*, 1804.
- [20] I. G. Richardson, *Cem. Concr. Res.* **2008**, *38*, 137.
- [21] J. Lee, D. Yoon, H. Cheong, *Nano Lett.* **2012**, *12*, 4444.
- [22] F. Babak, H. Abolfazi, G. Parviz, *Sci. World J.* **2014**, 276323.
- [23] T. Tanabe, K. Sakata, H. Mihashi, R. Sato, K. Maekawa, H. Nakamura, *Creep Shrinkage and Durability Mechanics of Concrete and Concrete Structures*, Taylor and Francis, London, UK **2009**.
- [24] N. B. Winter, *Understanding Cement: An Introduction to Cement Production, Cement Hydration and Deleterious Processes in Concrete*, Microanalysis Consultants, Woodbridge, UK 2012.
- [25] P. K. Mehta, P. J. M. Monteiro, in *Concrete: Microstructure, Properties, and Materials*, Prentice-Hall, Inc., Englewood Cliffs, NJ, USA **1993**, p. 165.
- [26] Y. Saez de Ibarra, J. J. Gaitero, E. Erkizia, I. Campillo, *Phys. Status Solidi A* **2006**, *203*, 6.
- [27] M. Konsta-Gdoutos, Z. Metaxa, S. P. Shah, *Cem. Concr. Compos.* **2010**, *40*, 7.
- [28] WBCSD, CSI Progress Report, **2012**.